Vibration energy harvesting device using P(VDF-TrFE) hybrid fluid diaphragm

Florian Huet, Fabien Formosa, Adrien Badel, Jean-Fabien Capsal, Mickaël Lallart

Vibration energy harvesting device using P(VDF-TrFE) hybrid fluid diaphragm

Florian Huet[a], Fabien Formosa[a], Adrien Badel[a], Jean-Fabien Capsal[b], Mickaël Lallart[b]

[a] *Univ. Savoie Mont Blanc. SYMME, F-74000 Annecy, FRANCE*
[b] *INSA de Lyon. LGEF, F-69100 Villeurbanne, FRANCE*

Abstract

We designed and realized a novel vibration energy harvester based on a P(VDF-TrFE) membrane. The mechanical arrangement consists in an incompressible fluid confined between two thin P(VDF-TrFE) piezoelectric membranes. It is called piezoelectric hybrid fluid diaphragm (PHFD). Compared with conventional vibration harvester, this solution appears to be simple and suitable for miniaturization and integration. The fluid-structure interaction allows a drastic reduction of the resonant frequency of the membrane whose mechanical tension is used to generate electrical power. Consequently, the realization of compact generators for low frequencies excitation (typically under 100 Hz) using membranes are possible. Moreover, nonlinear hardening behavior offers wideband capability. A theoretical model is established and allows the performance of the generator to be estimated. A first prototype has been fabricated and tested. The influence of the electric load,the amplitude and the frequency of the excitation on the voltage and the generated power have been investigated. A maximum output power of 158.33 μW per cubic centimeter of active material was obtained at 119.56 Hz for 40 m/s^2 amplitude acceleration.

Keywords: Vibration energy harvesting, Piezoelectric polymeric membrane, Fluid-structure interaction

Email address: Fabien.Formosa@univ-smb.fr (Fabien Formosa)

Nomenclature

b Nonlinear stiffness, N/m^3

C_0 Capacitance, F

C_j Constant

d Damping, N.s/m

d_{31} Piezoelectric coefficient, C/N

D_B Flexural stiffness, N.m

D_S Stretching stiffness, N/m

D_z Electric displacement, C/m^2

$\vec{e}_i$ Coordinate system (i refer to subscript)

E Diaphragm Young modulus, Pa

E_i Energy (i refer to subscript), J

E_z Electric field, V/m

f Frequency, Hz

h Diaphragm thickness, m

H Fluid height, m

$I, \dot{q}$ Current, A

k Linear stiffness, N/m

m_{mt} Inertial mass, kg

m_{tf} Moving fluid mass, kg

n Prestress stiffness, N/m

p Pressure, Pa

P Power, W

q Electrical charge, C

Q Quality factor

r Radial position, m

R Diaphragm radius, m

r_l Load resistance, Ω

R_{opti} Optimal resistance, Ω

t Time, s

u, u_{s0} Radial displacement, m

V Velocity, m/s

V_{elec} Voltage, V

$\dot{V}_{elec}$ Voltage derivative, V/s

V_{mec} External velocity, m/s

$\dot{V}_{mec}$ External acceleration, m/s^2

W_f Fluid work, J

w_s, u_s Unitary displacement

w Vertical displacement, m

x, X Membrane center displacement, m

$\dot{x}$ Membrane center velocity, m/s

$\ddot{x}$ Membrane center acceleration, m/m^2

z Vertical position, m

Greek Symbols

α, α_E, β Electromechanical coefficient, N/V

ε_{33} Relative permittivity

ε Strain

ε_0 Vacuum permittivity, F/m

ν Diaphragm Poisson coefficient

ρ_f Fluid density, kg/m^3

σ Stress, Pa

$\psi, \phi, \tilde{\phi}$ Velocity potential, m^2/s

ω Pulsation, rad/s

Subscripts

0 Initial or resonant

B Bending

$elec$ Electrical

f Fluid

L Linear

max maximum value

mec Mechanical

NL Nonlinear

$piezo$ Piezoelectric

r radial orientation

S Stretching

z Vertical orientation

θ Orthoradial orientation

1. Introduction

Wireless sensors networks (WSN) developments have increased over recent years. The potential implementation of these WSN in industrial, transportation or buildings applications could offer significant benefits: improved reliability integrating predictive maintenance, energy performance optimization using extensive collected information (temperature, humidity, electric consumption, ...). Because of the advancements of low-power WSN and MEMS technology, millimeter scale vibration harvesters (VEH) have attracted worldwide research interests [1]. VEH have been proposed using three main transduction principles: piezoelectric, electromagnetic and electrostatic [2, 3]. For the aforementioned applications, frequencies of typical ambient vibration sources are relatively low (typically less than 200 Hz) [4], which hinders the development of miniature VEHs.

Diaphragms like geometry are attractive to aim at simple and robust VEH. Moreover, low cost fabrication process can be envisioned for their mass production. Some prototypes have been proposed in the literature for vibration energy harvesting [5–7]. The 5 mm × 5 mm square membrane introduced in [5] shows a 2.4 kHz resonant frequency, while the harvester from [6], based on a 20.5 mm radius PZT buzzer, operates at 1.7 kHz. The very high resonant frequency of these devices prevents their use in realistic applications. Thus, some attempts have been made to solve the frequency issue by the addition of a bulky mass to the membrane. Chen proposed a 30 mm radius PZT buzzer with a bonded inertial mass estimated at 100 g [7]. It reduced the resonant frequencies in the 113 Hz range, but the integration capability of this structure is then hindered.

The membrane structures are also especially suitable for pressure energy harvesting. In this case, the excitation is no longer associated to vibration of the supporting structure but by the pressure fluctuation of any fluid. The imposed pressure excitation could lead to enhanced energy generation using optimized electrode distribution. Kim *et al.* [8–11] studied this route. They proposed analytical and experimental works to improve PZT piezoelectric membranes conversion when submitted to quasi-static pressure solicitations. The total stress due to bending and stretching is considered in the model to aim at a better anticipation of the generated power. But only quasi-static excitation is dealt with here.

PVDF (or similar materials P(VDF-TrFE), loaded PVDF, ...) is chosen as elec-

tromechanical transducer [12–15] in many VEH. The flexibility of this material is a major advantage for low frequency application, but its intrinsic performance is lower than PZT. The power density (considering the volume of piezoelectric material) from the studied literature [12–15] presents a range from 0.15 $\mu W/cm^3$ [13] to 195.12 $\mu W/cm^3$ for PVDF [14]. Such spread of values come from the quality of the PVDF material but also on the way the mechanical stress is induced in the material by the external excitations. For PZT diaphragm structures, literature shows a power density ranging from 15.04 mW/cm^3 [6] to 122.44 mW/cm^3 [7]. As expected the power density is much larger due to better material performance, but low frequency operations imply the use of a very large proof mass (122 g in [7]).

This work aims at demonstrating the modeling, the fabrication and testing of a new piezoelectric hybrid fluid diaphragm structure VEH. A diaphragm architecture aiming at the drastic reduction of the resonant frequency was proposed in [16]. It is based on an incompressible fluid encapsulated between two flexible membranes. The fluid dynamic inertia, when submitted to external excitations, generates hydraulic pressure on the diaphragms, resulting in a global low natural frequency and allowing their optimal deformation. Compared with similar structures with central mass introducing a rigid zone [7], the mechanical deformation is maximized here as the whole membrane is deformed. The assembly process would be simplified by using fluid as inertial fluid. Indeed, membrane are usually fragile due to their small thickness which make any mass addition a critical step. In this paper, single layered P(VDFTrFE) membranes are used to allow integrated transduction. This straightforward approach is justified because mechanical tension effect can be easily obtained for polymer membranes. As a result, the piezoelectric effect can be used with low complexity with respect to realization and electrical connection. The first part of the paper describes the VEH architecture and presents a complete theoretical electromechanical model. Realistic applications call for an efficient evaluation of a VEH performance potential under constrained background. Analytical is preferred here to a FEM approach because of the complexity of the device. In the case of the Piezoelectric Hybrid Fluid generator, a strongly coupled multiphysics model is indeed required: nonlinear membrane dynamic, piezoelectric and fluid-structure interactions have to be dealt with. The analytical approach eases the optimization step: Geometrical characteristics are used to simplify the model, which eventually

allow a low computation time evaluation of the generator performance. Complex effects, such as mechanical or fluid damping, geometrical flaws are not taken into account in the proposed analytical approach. These issues would however not be easily addressed by a FEM strategy, that would induce a larger simulation time. Simulation results for low and large excitation amplitudes are analyzed to underline the nonlinear behavior of the structure. In a second part, the realization and testing of a prototype are detailed. Finally, based on the comparison between the theoretical and the experimental results, an additional unexpected distortion effect is identified. The model is modified to allow future optimization. Further developments are finally suggested.

2. Theoretical modelling

2.1. Architecture

The architecture is based on the work of Formosa et al. [16] which demonstrates the possible use of fluid-membrane interaction to realize thick low resonant frequency membranes. It consists in an incompressible fluid confined between two thin membranes. The former is used as an inertial mass which allows a drastic reduction of resonant frequency for the global structure. The height of the device can be easily tuned to induce more or less inertia effect. The chosen fluid has to fulfill the trade-off between high density to enhance the fluid inertia effect and low viscosity to limit the potential mechanical dissipations. Here, the concept is developed to a further step by the integration of piezoelectric membranes for energy generation. The hybrid fluid diaphragm (HFD) structure is defined in the Fig. 1, which describes the architecture and it geometrical parameters.

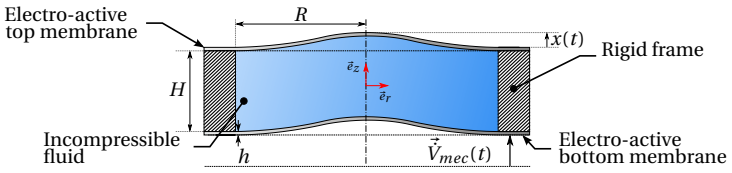

Figure 1: Schematic of the proposed structure HFD

The circular diaphragms are made from thin film P(VDF-TrFE). It is composed of a single piezoelectric material layer and top and bottom electrodes. The poling is or-

thogonal to the film plane. Table 1 defines the geometrical parameters and material properties of the system.

Due to the film structure and the electrodes' locations, flexural deformations induce a same amount of compressed and stretched piezoelectric material across the thickness and over the radius so the generated voltage is theoretically zero. However, large deformation amplitude generates stretching through the thickness that can be the major mechanical stress. Then, it produce an electrical voltage. This nonlinear behavior is the underlying principle of the proposed VEH.

Diaphragm properties (P(VDF-TrFE))

Radius (m)	R	Thickness (m)	h
Young modulus (Pa)	E	Poisson coefficient	ν
Piezoelectric coefficient (C/N)	d_{31}	Relative permittivity	ε_{33}

Fluid Properties (Glycerin)

Height (m)	H	Density (kg/m^3)	ρ_f

Table 1: Main parameters of the PHFD

2.2. Analytical model

The model in [16] was based on the Ritz method to obtain approximate solutions for both the fluid motion and the diaphragms' deformation. In the present work, this mechanical model is simplified and the piezoelectric membrane behavior is added. Indeed, from the mechanical point of view, the final dynamic behavior (*i.e* the first resonant frequency) of the HFD is notably lower than the first natural frequency of a diaphragm alone. Therefore, a simple static behavior description of the membrane can be used for approximation of the mechanical solution instead of the first modal shapes as it was done in the previous model. Additionally, the frame displacement is introduced which is in line with the vibration energy harvesting application background of this work.

The modified modeling strategy is developed hereafter using the following assumptions:

- Clamped edge mechanical boundary condition.

- Same geometry and materials properties for each membranes.
- The initial prestress of the diaphragm is taken into account considering an initial uniform radial displacement u_{S0} applied on the membranes' rim.
- Large strain is considered.
- The shear stress is neglected.
- The fluid is incompressible and inviscid.
- The fluid motion is assumed to be irrotational [17].
- Axially symmetric motions.
- Diaphragms have the same displacement (in-phase motion).
- The polarization direction is along the normal of the diaphragms ($\vec{e}_z$).

2.2.1. Mechanical approximate static solution

The transverse and radial deformations of the diaphragm can be written as the quasi-static solution under uniform pressure [18]:

$$\begin{aligned} w(t,r) &= x(t)\,w_s(r) = x(t)\left(1-\left(\frac{r}{R}\right)^2\right)^2 \\ u(t,r) &= x(t)^2 u_s(r) = \frac{x(t)^2}{126R^3}\,r\,(R-r)\left((179-89\nu)+\frac{3}{R}\,(-79+13\nu)\,r\right) \end{aligned} \tag{1}$$

In which $w(t,r)$ is the deflection of the diaphragms along the vertical direction ($\vec{e}_z$). $u(t,r)$ is the radial displacement along $\vec{e}_r$. $x(t)$ is the maximal relative with respect to its clamped rim vertical displacement at the center of one diaphragm.

2.2.2. Fluid equations and approximate solution

As the liquid motion is assumed to be irrotational, its velocity $\vec{V}_f(t,r,z)$ can be associated to a velocity potential $\psi(t,r,z)$ defined such as:

$$\vec{V}_f(t,r,z) = \vec{\nabla}\psi(t,r,z) \tag{2}$$

In which $\vec{\nabla}$ is the gradient operator. In order to take into account the vertical velocity of the entire frame ($V_{mec}(t)$ in Fig. 1) and in a case of small relative motion, a new velocity potential $\phi(t,r,z)$ is defined as:

$$\vec{V}_f(t,r,z) = \vec{V}_{mec}(t) + \vec{\nabla}\phi(t,r,z) = \vec{\nabla}\psi(t,r,z) = \vec{\nabla}(V_{mec}(t)z + \phi(t,r,z)) \tag{3}$$

Finally, the equilibrium equation for the liquid results in:

$$\vec{\nabla}^2\phi(t,r,z) = 0,\ \forall\ r \in [0,R]\ \ and\ \forall\ z \in \left[-\frac{H}{2}, \frac{H}{2}\right] \tag{4}$$

In which $\vec{\nabla}^2$ is the Laplace operator. Based on the solution of the transcendental Eq. 4, the general form of the fluid velocity potential is:

$$\phi(t,r,z) = \sum_{j=1}^{N} (C_j(t)\sinh(k_j z)) J_0(k_j r) \tag{5}$$

In which N is the number of retained fluid modes $J_0(k_j r)$ is the Bessel first kind function and k_j is the j_{th} root of Eq. 4. $C_j(t)$ is a parameter which depends on the velocity of the diaphragm center ($\dot{x}$).

The boundary conditions for the fluid can be expressed as:

$$\begin{aligned} &\vec{V}_f.\vec{e}_r = 0,\ for\ r = R\ and\ \forall\ z \in \left[-\frac{H}{2}, \frac{H}{2}\right] \\ &\vec{V}_f.\vec{e}_z = \left(\frac{dw}{dt} + V_{mec}\right),\ for\ z = \pm\frac{H}{2}\ and\ \forall\ r \in [0,R] \end{aligned} \tag{6}$$

Using Eq. 1 and Eq. 3, the boundary conditions from Eq. 6 are written again as:

$$\begin{aligned} &\frac{\partial\phi}{\partial r} = 0,\ for\ r = R\ and\ \forall z \in \left[-\frac{H}{2}, \frac{H}{2}\right] \\ &\frac{\partial\phi}{\partial z} = \dot{x}w_s,\ for\ z = \pm\frac{H}{2}\ and\ \forall r \in [0,R] \end{aligned} \tag{7}$$

For developing the weak form solutions of Eq. 7, we define the new function $\tilde{\phi}(t,r,z) = C_0(t) + \phi(t,r,z)$ and integrate it over the whole fluid domain:

$$\begin{aligned} &-\int_{-\frac{H}{2}}^{\frac{H}{2}}\int_0^R \left(\frac{\partial\phi}{\partial r}\frac{\partial\tilde{\phi}}{\partial r} + \frac{\partial\phi}{\partial z}\frac{\partial\tilde{\phi}}{\partial z}\right) r\,dr\,dz + 2\int_0^R \dot{x}w_s\tilde{\phi}\left(R, \frac{H}{2}\right) r\,dr = 0, \\ &\forall\ \tilde{C}_j,\ j = 0..N \end{aligned} \tag{8}$$

Solving Eq. 8, N is chosen such as the boundary condition at the diaphragm surface is satisfied with a sufficient accuracy. Using $N = 3$ actual deformed shape of the membrane is matched [16].

The fluid pressure can be expressed using the Cauchy-Lagrange equation for unsteady flow:

$$\rho_f \frac{\partial \psi}{\partial t} + \frac{1}{2}\rho_f V_f^2 + p = constant \tag{9}$$

Where ρ_f is the fluid density. Eq. 9 is developed using Eq. 3. For simplification purpose, the relative weights between the terms are assessed defining the dimensionless variables given in table 2.

Attribute	Length		Time	Velocity potential
Variable	r	z	t	ϕ
Reference value	R	H	$\frac{V_{mec}}{h}$	hV_{mec}
Dimensionless variable	$r^* = \frac{r}{R}$	$z^* = \frac{z}{H}$	$t^* = \frac{ht}{V_{mec}}$	$\phi^* = \frac{\phi}{hV_{mec}}$

Table 2: Definition of the dimensionless variables

The dimensionless expression of Eq. 9 is then:

$$\rho_f \left(\frac{\partial \phi^*}{\partial t^*} + \dot{V}_{mec} \frac{Hz^*}{h^2} \right) + \frac{1}{2}\rho_f \left(\left(\frac{V_{mec}}{R} \frac{\partial \phi^*}{\partial r^*} \right)^2 + \left(\frac{V_{mec}}{H} \frac{\partial \phi^*}{\partial z^*} \right)^2 + \frac{V_{mec}^2}{h^2} \right) + \frac{p}{h^2} = constant \tag{10}$$

Considering the size of the considered structure (Table 5) and Eq. 10, the first and second order terms $\left(\frac{\partial \phi}{\partial r}\right)^2$, $\left(\frac{\partial \phi}{\partial z}\right)^2$ are neglected.

At the whole fluid domain frontier ($r = R$) the constant right hand term of Eq. 10 is null, so the pressure can be finally written as:

$$p = -\rho_f \left(\frac{\partial \phi}{\partial t} + \dot{V}_{mec} z \right) - \frac{1}{2}\rho_f {V_{mec}}^2 \tag{11}$$

The joint effects of the global motion of the fluid (V_{mec}) and the local perturbation is clearly established by Eq. 11: the frame motion acts as a buoyancy force on the membranes.

2.2.3. Global dynamic equilibrium

The dynamic equilibrium equations are obtained using the Energy method applied to each of the piezoelectric diaphragms. The model is detailed for the bottom

diaphragm. The procedure is same for the top one.

The piezoelectric constitutive relations are:

$$\begin{aligned}
\sigma_r &= \frac{E}{1-\nu^2}(\varepsilon_r + \nu\varepsilon_\theta - d_{31}E_z(1+\nu)) \\
\sigma_\theta &= \frac{E}{1-\nu^2}(\varepsilon_\theta + \nu\varepsilon_r - d_{31}E_z(1+\nu)) \\
D_z &= -d_{31}\frac{E}{1-\nu}(\varepsilon_r + \varepsilon_\theta) + \varepsilon_{33}\varepsilon_0 E_z
\end{aligned} \tag{12}$$

The strain components can be expressed distinguishing the linear bending and the nonlinear stretching behaviors [19] such as:

$$\begin{aligned}
\varepsilon_r &= \varepsilon_{rL} + \varepsilon_{rNL} \\
&= -x(t)z\frac{d^2w_s(r)}{dr^2} + x^2(t)\left(\frac{du_s(r)}{dr} + \frac{1}{2}\left(\frac{dw_s(r)}{dr}\right)^2\right) \\
\varepsilon_\theta &= \varepsilon_{\theta L} + \varepsilon_{\theta NL} \\
&= -x(t)\frac{z}{r}\frac{dw_s(r)}{dr} + x^2(t)\frac{u_s(r)}{r}
\end{aligned} \tag{13}$$

Using Eq. 12 and Eq. 13, the bending and stretching energies (E_{mecB} and E_{mecS} respectively) are derived. The linear and nonlinear stiffness coefficients k and b are finally defined as:

$$\begin{aligned}
E_{mecB} &= \frac{1}{2}\frac{E}{1-\nu^2}\int_0^R\int_{-\frac{h}{2}}^{\frac{h}{2}}\int_0^{2\pi}(\varepsilon_{rL}^2 + 2\nu\varepsilon_{rL}\varepsilon_{\theta L} + \varepsilon_{\theta L}^2)rdrdzd\theta \\
&= \frac{1}{2}x^2 2\pi D_B\int_0^R\left(\left(\frac{d^2w_s}{dr^2}\right)^2 + \frac{1}{r^2}\left(\frac{dw_s}{dr}\right)^2 + \frac{2\nu}{r}\frac{dw_s}{dr}\frac{d^2w_s}{dr^2}\right)rdr \\
&= \frac{1}{2}x^2k
\end{aligned} \tag{14}$$

$$\begin{aligned}
E_{mecS} &= \frac{1}{2}\frac{E}{1-\nu^2}\int_0^R\int_{-\frac{h}{2}}^{\frac{h}{2}}\int_0^{2\pi}(\varepsilon_{rNL}^2 + 2\nu\varepsilon_{rNL}\varepsilon_{\theta NL} + \varepsilon_{\theta NL}^2)rdrdzd\theta \\
&= \frac{1}{2}x^4 2\pi D_S\int_0^R\left(\left(\frac{du_s}{dr} + \frac{1}{2}\left(\frac{dw_s}{dr}\right)^2\right)^2 + 2\nu\left(\frac{du_s}{dr} + \frac{1}{2}\left(\frac{dw_s}{dr}\right)^2\right)\left(\frac{u_s}{r}\right) + \left(\frac{u_s}{r}\right)^2\right)rdr \\
&= \frac{1}{2}x^4b
\end{aligned} \tag{15}$$

In which, $D_B = \frac{Eh^3}{12(1-\nu^2)}$, $D_S = \frac{Eh}{(1-\nu^2)}$. The initial prestress of the diaphragm associated to the assembly procedure is taken into account. The ensuing in-plane radial

and orthoradial stresses are:

$$\sigma_{rS0} = \sigma_{\theta S0} = \frac{E}{(1-\nu)} \frac{u_{S0}}{R} \tag{16}$$

From Eq. 16, the prestress mechanical energy is:

$$\begin{aligned} E_{mecS0} &= \frac{1}{2} \int_0^R \int_{-\frac{h}{2}}^{\frac{h}{2}} \int_0^{2\pi} (\sigma_{rS0}\varepsilon_{rNL} + \sigma_{\theta S0}\varepsilon_{\theta NL}) r dr dz d\theta \\ &= \frac{1}{2} x^2 2\pi \frac{E}{1-\nu} \frac{u_{S0}}{R} \int_0^R \left(\frac{du_s}{dr} + \frac{1}{2} \left(\frac{dw_s}{dr} \right)^2 + \frac{u_s}{r} \right) r dr \\ &= \frac{1}{2} x^2 n \end{aligned} \tag{17}$$

The prestress linear stiffness n is deduced from Eq. 17. Finally, the mechanical work of the fluid dynamic pressure upon the diaphragm is:

$$\begin{aligned} W_f &= -x 2\pi \rho_f \int_0^R w_s \left(\frac{\partial \bar{\phi}}{\partial t} - \frac{H}{2} \dot{V}_{mec} + \frac{1}{2} {V_{mec}}^2 \right) r dr \\ &= -x \left(m_{mf} \ddot{x} + \frac{m_{tf}}{H} \left(-H \dot{V}_{mec} + \frac{1}{2} {V_{mec}}^2 \right) \right) \end{aligned} \tag{18}$$

In which m_{mf} is the fluid inertial mass and m_{tf} is the fluid total (static) mass.

The electric field E_z can be expressed as a function of the electric potential (V_{elec}) such as: $E_z = \frac{V_{elec}}{h}$. The stretching of the structure induces in-plane strain. The piezoelectric coupling energy E_{piezo} is then expressed as:

$$\begin{aligned} E_{piezo} &= -\frac{1}{2} D_s (1+\nu) d_{31} \frac{V_{elec}}{h} \int_0^R \int_{-\frac{h}{2}}^{\frac{h}{2}} \int_0^{2\pi} (\varepsilon_{rNL} + \varepsilon_{\theta NL}) r dr \\ &= -\frac{1}{2} 2\pi D_S (1+\nu)_{31} \frac{V_{elec}}{h} \int_0^R \left(\frac{du_s}{dr} + \frac{1}{2} \left(\frac{dw_s}{dr} \right)^2 + \frac{u_s}{r} \right) r dr \\ &= \frac{1}{2} x^2 \alpha \frac{V_{elec}}{h} \end{aligned} \tag{19}$$

In which α is the piezoelectric force factor.

Finally, the dynamic equilibrium equation for the bottom diaphragm is given by:

$$\frac{\partial}{\partial x} \left(E_{mecB} + E_{mecS} + E_{piezo} + E_{mecS0} + W_f \right) = 0 \tag{20}$$

Using Eq. (7-8), Eq. (11-15) and Eq. (17-19) to write again Eq. 20, the dynamic equilibrium equation for the bottom diaphragm is:

$$m_{mf} \ddot{x} + d\dot{x} + (k+n)x + 2bx^3 + \alpha \frac{x}{h} V_{elec} = m_{tf} \dot{V}_{mec} - \frac{1}{2} \frac{m_{tf}}{H} {V_{mec}}^2 \tag{21}$$

In which the dissipation can be introduced as an equivalent viscous damping coefficient (d) such as:

$$d = \frac{m_{mf}}{Q}\omega_0 = \frac{\sqrt{m_{mf}(k+n)}}{Q} \tag{22}$$

Where Q is the estimated mechanical quality factor of the structure in the case of small amplitude vibration. Applying the same procedure, the top diaphragm equilibrium equation is:

$$m_{mf}\ddot{x} + d\dot{x} + (k+n)x + 2bx^3 + \alpha\frac{x}{h}V_{elec} = m_{tf}\dot{V}_{mec} + \frac{1}{2}\frac{m_{tf}}{H}{V_{mec}}^2 \tag{23}$$

From Eq. 21 the linear case (small amplitude and closed circuit condition) natural pulsation can be written as:

$$\omega_0 = \sqrt{\frac{k+n}{m_{mf}}} \tag{24}$$

To support the quasi-static approximation, ω_0 is compared to the theoretical natural pulsation calculated from the previous model [16] using the same geometry and material properties. Table. 3 presents the frequencies and the discrepancies between the two models for various membrane thicknesses.

Attribute	Value				
Thickness h (µm)	20	25	40	50	110
Dynamic model [16] f_0 (Hz)	5.486	7.664	15.494	21.637	70.298
Static model f_0 (Hz)	5.479	7.658	15.498	21.659	70.677
Difference (%)	-0.127	-0.079	0.029	0.103	0.539

Table 3: Comparison of natural frequencies results from the two proposed models

The similarity of the results demonstrates that the simplification of previous model is relevant in the case of the proposed structure.

2.2.4. Electrical equation

The electric equilibrium equation can be derived from:

$$\frac{\partial}{\partial V_{elec}}E_{elec} = -q \tag{25}$$

Where q is the electrical charges so that $\dot{q}$ is the generated current (I).

Using the piezoelectric constitutive relations Eq. 12, the electrical energy E_{elec} is written as:

$$\begin{aligned} E_{elec} &= \frac{1}{2} 2\pi \int_0^R D_z E_z r dr \\ &= \frac{1}{2} 2\pi \int_0^R \left(\varepsilon_{33} \varepsilon_0 \frac{V_{elec}}{h} - d_{31}(\sigma_r + \sigma_\theta) \right) \frac{V_{elec}}{h} r dr \\ &= \frac{1}{2} \left(C V_{elec}^2 - \alpha_E x^2 \frac{V_{elec}}{h} \right) \end{aligned} \tag{26}$$

E_{elec} is the addition of two terms: the stored energy in the capacitance (C_0) and the piezoelectric coupling related to the coupling factor (α_E). Using Eq. (12, 13) and Eq. 25, one can demonstrate the equality $\alpha = \alpha_E$. From Eq. 25 and Eq. 26 the electrical equilibrium equation is finally written as:

$$C_0 V_{elec} - \frac{1}{2} \alpha \frac{x}{h} x = -q \tag{27}$$

Performing the time derivation of Eq. 27:

$$-C_0 \dot{V}_{elec} + \alpha \frac{x}{h} \dot{x} = I \tag{28}$$

Eq. 28 underlines the voltage generation due to the large deformation of the membranes as small displacements (x) lead to second order values of the piezoelectric coupling term (second term of the left hand side of Eq. 28). It can also be deducted from Eq. 28 that in open circuit condition, the voltage is proportional to x^2. The piezoelectric voltage frequency is then two times the excitation frequency, which is a another particular feature of the proposed concept.

Eq. 21 and Eq. 28 describe the electromechanical behavior of the PHFD. This lumped model can be summarized by the schematic of Figure. 2. The mechanical part of the system (Fig. 2a) can be read as a moving fluid mass (m_{mf}) linked to a linear spring (LS) whose stiffness is $(k+n)$ accounting for the flexural diaphragm stiffness and two nonlinear springs (NLS) whose total stiffness equals $2b$. The latter are related to the nonlinear stretching associated to large amplitude motions of the diaphragms. The piezoelectric conversion coefficient (α) is parallel to the NLS. The input force is $m_{tf} \dot{V}_{mec}$ with $\dot{V}_{mec}$ the frame acceleration. One single damper (d) stands for all the mechanical losses (the viscous losses within the membrane

plus the fluid dissipation). The obtained piezoelectric generator behaves as a voltage source whose value is proportional to the product of the diaphragm central displacement and velocity (Fig. 2b).

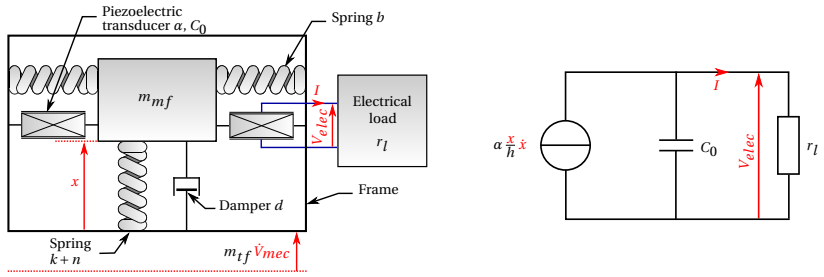

(a) Mechanical model (b) Electrical model

Figure 2: Nonlinear inertial generator electromechanical modeling

Table 4 details the whole model parameters, their units and relationship to the geometry and material properties. It is worthy of note that the stiffness property is independent to the mass property in the obtained structure, which is an advantage for optimization.

Parameter	Symbol	Relation	Unit
Fluid inertial mass	m_{mf}	See [16] $f(\rho_f, H, R)$	kg
Fluid excitation mass	m_{tf}	$\frac{H\pi\rho_f R^2}{12}$	kg
Flexural stiffness	k	$\frac{32\pi Eh^3}{9R^2(1-\nu^2)}$	N/m
Tension stiffness	b	$\frac{\pi Eh(7505+4250\nu-2791\nu^2)}{39690R^2(1-\nu^2)}$	N/m^3
Electromechanical coefficient	α	$-\frac{4\pi Ed_{31}}{3(1-\nu)}$	N/V
Diaphragm capacitance	C_0	$\varepsilon_{33}\varepsilon_0\frac{\pi R^2}{h}$	F
Prestress flexural stiffness	n^*	$\frac{4u_{S0}\pi Eh}{3R(1-\nu^2)}$	N/m
Damping coefficient	d	$\frac{\sqrt{m_{mf}(k+n^*)}}{Q^*}$	N.s/m

* Measured values

Table 4: Model parameters relation

2.2.5. Simulation results

Table 5 gives the geometry and material properties values used in the simulations. They are those of the prototype presented in section 3.

Diaphragm properties (P(VDF-TrFE))

R	10 mm	h	84 µm
E	1 GPa	ν	0.34
d_{31}	−5 pC/N	ε_{33}	8.25

Fluid Properties (Glycerin)

H	20 mm	ρ_f	1260 kg/m^3

Table 5: Geometry and material properties of the PHFD

2.2.6. Acceleration

Fig. 3a shows the evolution of the LS and NLS forces according to the normalized displacement of the membrane center. The threshold from which the NLS effect is no more negligible compared to the LS one is estimated at 10 % of the LS force. It is reached when the displacement is about two times the thickness of the membrane ($x \approx 172.6$ µm). Fig. 3b plots the displacement evolution with respect to the acceleration amplitude ($\dot{V}_{mec}$). The nonlinear mechanical behavior appears at an acceleration of approximately 13 m/s^2, which is the value required to reach the aforementioned threshold. The NLS effect becomes predominant at 34 m/s^2 (for 50 % of LS contribution). Between these two limits a transition area is identified. Consequently, the acceleration value chosen for simulations is of 40 m/s^2. It allows large strains to be reached and nonlinear effect to be clearly observed and compared to the theoretical model.

2.2.7. Displacement and power

The first results are based on the parameters defined in table 4 and table 5. In order to characterize the harvester performance, we carry out simulations using a slow frequency sweep ranging from 80 Hz to 140 Hz and a varying electrical load resistance r_l (from 0.6 MΩ to 14 MΩ).

Fig. 4a shows the displacement of the membrane center (x) and the generated power with respect to the electrical load resistance and the excitation frequency.

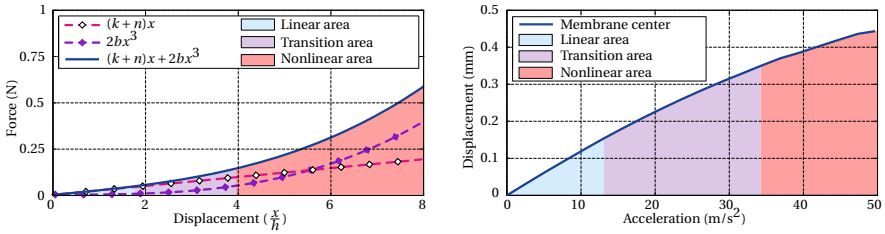

(a) Stiffness forces

(b) Acceleration setup

Figure 3: Linear / nonlinear limits

One can observe the typical response associated to the mechanical nonlinear hardening behavior. Moreover, the electromechanical conversion has a weak impact on the mechanical behavior, which is in line with the anticipated low electromechanical coupling obtained from the use of P(VDF-TrFE) material. This simulation reveals a 130.31 Hz resonant frequency and a 456.2 µm maximum displacement. The harvester power behavior (Fig. 4b) exhibits a peak power of 4.48 µW at $f = 130.31$ Hz (matching the maximum displacement) for an optimal load resistance of 2.21 MΩ. This value corresponds to the matching load for a voltage frequency equals to $2 \times f$ so $R_{opti} = \frac{1}{4\pi f C_0}$.

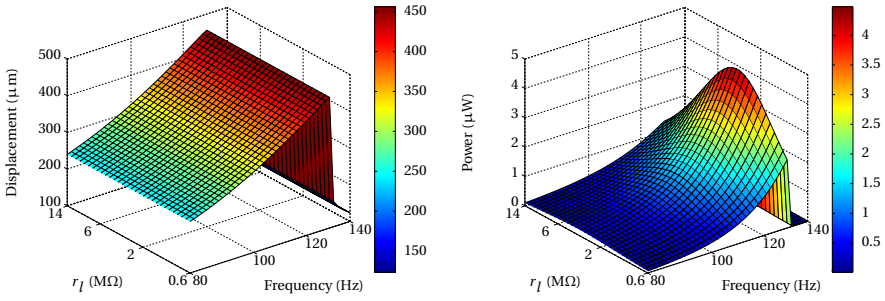

(a) Displacement

(b) Power

Figure 4: Theoretical simulation results

3. Experimental approach

3.1. Prototype description and experimental setup

3.1.1. Prototype

A PHFD prototype has been realized. Its purpose is the validation of the proposed model. Its dimensions and properties are given in table 5. Fig. 5a presents a CAD section of the HFD design, while Fig. 5b shows the realized prototype.

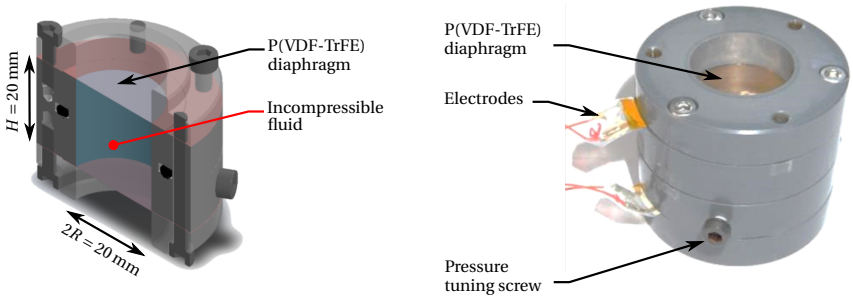

(a) CAD design (b) Realisation

Figure 5: HFD prototype

P(VDF-TrFE) was selected because it presents the best ration between piezoelectric performance and flexibility [20]. They were made from a solution of Poly(VinyliDene-Fluoride-co-TriFluoroEthylen. Compared with the use of commercial PVDF films, it allowed us to define customized thickness. It also authorizes more margin for future explorations of other dimensions or electrode optimization. The thickness variations of the obtained films are of a few microns over square a surface of 20 mm × 20 mm. Glycerin is chosen as the fluid for its high density though its dynamic viscosity is high.

An assembly procedure has been defined to guarantee the proper assemblage, the membrane assemblage and the fluid filling. The first step is the clamping of the membranes to obtain two symmetrical parts of the final PHFD. This operation is realized without fluid. The membranes are stretched over a low shoulder to aim at flat surfaces and reduce the film wrinkles. This operation induces mechanical prestress (coefficient n in Eq. 21). It is worthy of note that the design of the shoulder could be used to control the induced prestress to a desired value. This study has not been performed yet as it is beyond the scope of the paper.

The next step is to put the two parts together when immersed into the chosen fluid to get a filled HFD without bubbles to guarantee incompressibility. The tightness is provided by an O-ring as can be seen in Fig. 5a. The internal fluid pressure, and consequently the flatness of the diaphragms can be tuned using a screw (Fig. 5b). Indeed, the slight squeeze of the O-ring associated to the incompressibility of the fluid turn any volume modification into static pressure variation.

3.1.2. Experimental setup

The piezoelectric PHFD was tested on an electrodynamic shaker driven by a slow varying increasing frequency signal similar to the used simulations excitation. Using an accelerometer and a dedicated control unit, a closed-loop control ensures constant acceleration amplitude of the shaker over the frequency range. The displacement and velocity of the top diaphragm center are measured using a differential laser vibrometer. The control unit also drives a set of electric load resistance (r_l) ranging from 0.6 MΩ to 14 MΩ. Different acceleration levels (from 30 m/s^2 to 60 m/s^2) allowing the nonlinear behavior to be triggered have been used.

3.2. Experimental results

3.2.1. Displacement and power

The experimental results are shown in Fig. 6 to be compared to Fig. 4 for an acceleration amplitude of 40 m/s^2. The nonlinear effect associated to large displacements is clearly visible (Fig. 6a) while the electromechanical conversion has a negligible impact. The displacement amplitude at the resonant frequency is 376.5 μm, which is more than four times the thickness of the membrane. Fig. 6b plots the power response. Its maximum is about 4.18 μW at the resonant frequency and for a 2.88 MΩ load resistance. It is worthy of note that the mechanical hardening effect leads to a large bandwidth of about 40 Hz. The power density (calculated with respect to the volume of piezoelectric material) of the proposed generator is 158.33 $\mu W/cm^3$, which is in the order of magnitude of P(VDF-TrFE) VEH performances reported in the literature.

3.2.2. Temporal results

The temporal results underline the frequency doubling voltage in accordance with Eq. 28. This is clearly visible comparing the blue line (displacement of the

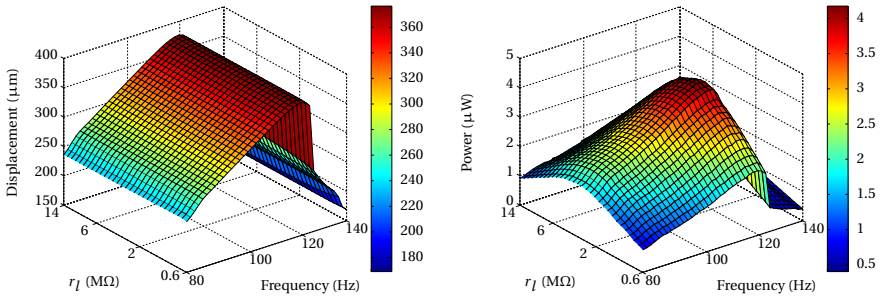

(a) Displacement

(b) Power

Figure 6: Experimental performances at 40 m/s^2

membrane center at 119.6 Hz) and the red dashed line (voltage) in Fig. 7a. However, the Fourier transform of the voltage signal (red dashed line in Fig. 7b) reveals two dominant harmonics: the first is at the diaphragm displacement frequency (blue plain line in Fig. 7b) and can be related to a voltage produced by the bending motion whereas the second is at about twice this frequency (224.2 Hz) and is the expected nonlinear behavior. An ideal piezoelectric membrane does not present electrical generation associated to bending motion as stated by the theoretical model. Hence, the first harmonic is thought to be induced by an energy generation due to the membranes bending. This observation highlights what is thought to be the non-ideal flat geometry of the membranes, which was not taken into account in the model. Indeed, tiny residual wrinkles are likely to bring complex mechanical neutral plane shape which could induce piezoelectric voltage for flexural deformations. However, this effect is not detrimental as it tends to increase the generated voltage.

4. Model / experiment comparison and optimization

The aim of this section is to validate the theoretical model so it could be used as an optimization tool for the design of PHFD generators. Moreover, the identification procedure is mandatory for the dissipation of the prestress of the membrane. Yet, the first prototype may present some specificity which are likely to generate discrepancies between the theoretical and experiment results. An empirical law would have to be established based on multiple prototypes. Therefore, an identification strategy of the model parameters is proposed here and the variations with the theo-

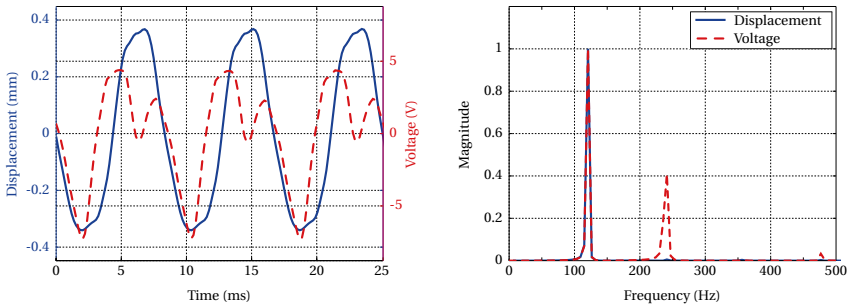

(a) Temporal

(b) Fourier transform

Figure 7: Experimental displacement and voltages signals at 40 m/s^2

retical model are carefully assessed.

4.1. Parameters identification

The mechanical behavior of the device is virtually not changed by the electric behavior considering the low coupling coefficient of the polymer piezoelectric film. Therefore, the identification is performed in two steps. The first one is to identify the mechanical parameters m_{tf}, m_{mf}, b, n and Q. It is assumed that a reliable value of k is obtained from the theoretical approach. The prestress value n may be shifted with different tightenings of the membrane and has to be experimentally identified. The identification procedure is to minimize the difference between the simulated and experimental displacement when varying the excitation frequency for a fixed given electrical load ($r_l = r_{peakpower}$). The least square method is used.

The second step is to identify the electrical behavior by adjusting the two parameters α and C_0. The chosen strategy is slightly different here as two sets of reference results are used: i) The generated power when varying frequencies for a given load resistance ($r_l = r_{peakpower}$); ii) The power at a given frequency ($f = f_{peakpower}$) when varying the electrical load resistance.

The choice of the power results provides a characteristic point (peak power) with more information than the voltage. Indeed, the voltage alone does not allow to accurately determine the α and C_0 parameters, because there may be several valid parameters' values sets for a given frequency. The sum of the normalized differences between experimental and simulated results defines the objective function to be minimized by the least square method.

This identification procedure has been firstly applied assuming that the "bending voltage" is negligible compared to the "stretch voltage". A rather good model-testing correlation is obtained on both the mechanical (Fig. 8a) and electrical (Fig. 8b) responses.

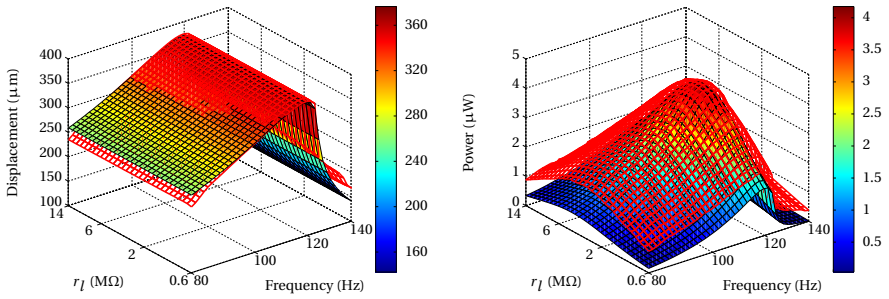

(a) Displacement

(b) Power

Figure 8: Optimized simulation (color scale) and experimental (red mesh) results comparison

Table 6 shows the principal features of the VEH with relative error between experimental and simulation results. The errors are acceptable (< 10 %), except for the bandwidth with a maximal discrepancy of 42.12 %.

	f_0	P_{max}	X_{max}	R_{opti}	$Bandwidth$
Exp	119.56 Hz	4.17 µW	376.5 µm	2.88 MΩ	40.28 Hz
Simu	119.56 Hz	4.09 µW	373.6 µm	2.88 MΩ	23.31 Hz
Error	0 %	−1.92 %	−0.77 %	0 %	−42.13 %

Table 6: Comparison between experimental and simulation results with first identified parameter set

The power responses (Fig. 8b) present a larger divergence for values distant from the power peak. As mentioned before, the experimental measured signal is composed mainly of two harmonics (see Fig. 9a). In Fig. 9b, a Fourier transform allows these frequencies to be read as 119.56 Hz and 239.12 Hz. This voltage generation for bending motion is identified as the result of a slight initial bending of the membrane. As it is considered here as a unexpected behavior, the model has not been deeply modified. Yet, an additional linear piezoelectric electromechanical coefficient (β) is introduced and identified in the following to validate the interpretation.

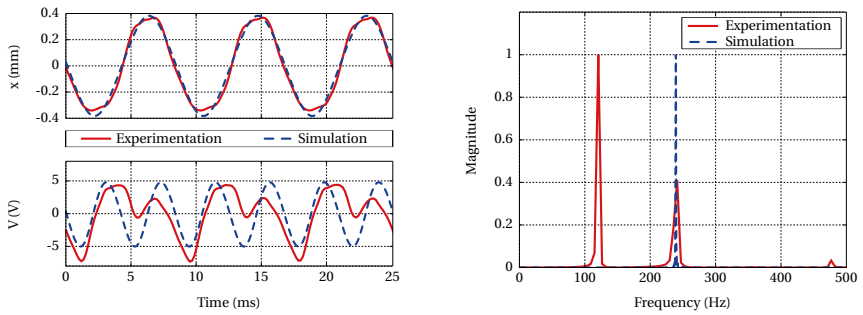

(a) Temporal displacement and voltage

(b) Voltage Fourier transform

Figure 9: Optimized simulation and experimental signals comparison

The modified model is defined by the set of coupled equations (Eq. 29).

$$\begin{aligned} &m_{mf}\ddot{x} + d\dot{x} + (k+n)x + 2bx^3 + \beta V_{elec} + \alpha\frac{x}{h}V_{elec} = m_{tf}\dot{V}_{mec} \\ &-C_0\dot{V}_{elec} + \beta\dot{x} + \alpha\frac{x}{h}\dot{x} = I \end{aligned} \tag{29}$$

A schematic representation of the model using for Eq. 29 is given in Fig. 10.

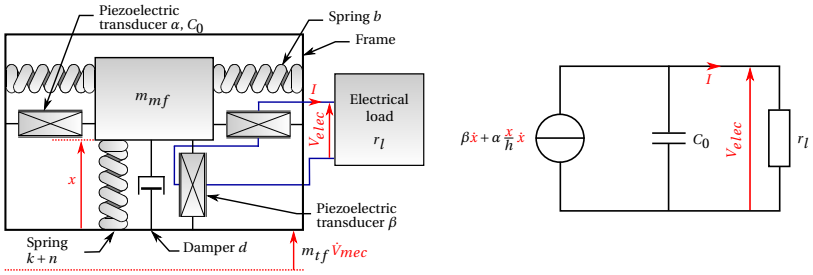

(a) Mechanical model

(b) Electrical model

Figure 10: Nonlinear inertial generator modeling with flexural effect

Because of the negligible impact of the electrical behavior on the mechanical behavior, only the electrical parameters (α, C_0 and β) are identified again using the strategy described above. It can be seen from Fig. 11b that the overall difference between the simulated and experimental results has decreased. The bandwidth error decrease (table 7) is in accordance with this observation. Fig. 11a and 11c show a much better agreement between the experimental and simulated temporal dis-

placement and voltages. The α and C_0 parameters are also closer to those determined by the theoretical model (Table 7).

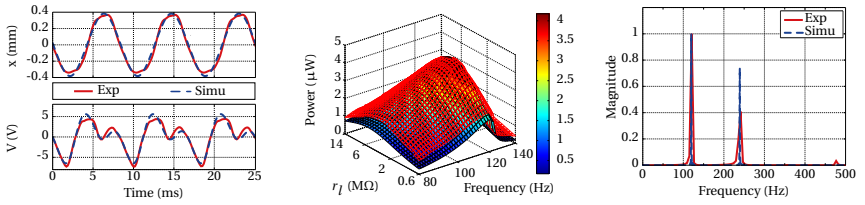

(a) Temporal signals (b) Power (c) Voltage Fourier transform

Figure 11: Optimized simulation with flexural effect and experimental results comparison

	f_0	P_{max}	X_{max}	R_{opti}	$Bandwidth$
Exp	119.56 Hz	4.17 µW	376.5 µm	2.88 MΩ	40.28 Hz
Simu	119.56 Hz	4.11 µW	373.6 µm	2.88 MΩ	28.39 Hz
Error	0 %	−1.43 %	−0.77 %	0 %	−29.52 %

Table 7: Comparison between experimental and second identified parameter set simulation results

4.2. Effect of the acceleration and identified model validation

For further investigations, we compared the simulated and experimental results for two different accelerations (30 m/s^2 and 60 m/s^2) using the identified parameters. For the lowest acceleration case the correlation is slightly deteriorated, but the qualitative response is captured (Fig. 12b). The power is underestimated (Table 8). For this level of acceleration, the generator response is close to a linear system behavior. The suspected "imperfections" of the membrane create important and complex effects associated with bending, for which coefficient β alone cannot represent.

	f_0	P_{max}	X_{max}	R_{opti}	$Bandwidth$
Exp	112.91 Hz	3.01 µW	315.5 µm	2.88 MΩ	32.85 Hz
Simu	111.29 Hz	2.13 µW	302.1 µm	3.58 MΩ	22.87 Hz
Error	−1.43 %	−29.23 %	−4.25 %	+24.31 %	−30.38 %

Table 8: Comparison between experimental and optimized simulation results at 30 m/s^2 of acceleration

For the high acceleration case for which the nonlinear behavior dominates the response, the comparison is better. The performance criteria are validated (Ta-

ble 9) with an error of 13.92 % for the power. The overall difference between is lower
395 (Fig. 12c and Fig. 12d).

	f_0	P_{max}	X_{max}	R_{opti}	$Bandwidth$
Exp	132.21 Hz	9.34 µW	475.8 µm	2.58 MΩ	38.28 Hz
Simu	136.04 Hz	10.64 µW	487.5 µm	2.31 MΩ	28.12 Hz
Error	+2.89 %	+13.92 %	+2.46 %	−10.45 %	−26.54 %

Table 9: Comparison between experimental and optimized simulation results at 60 m/s^2 of acceleration

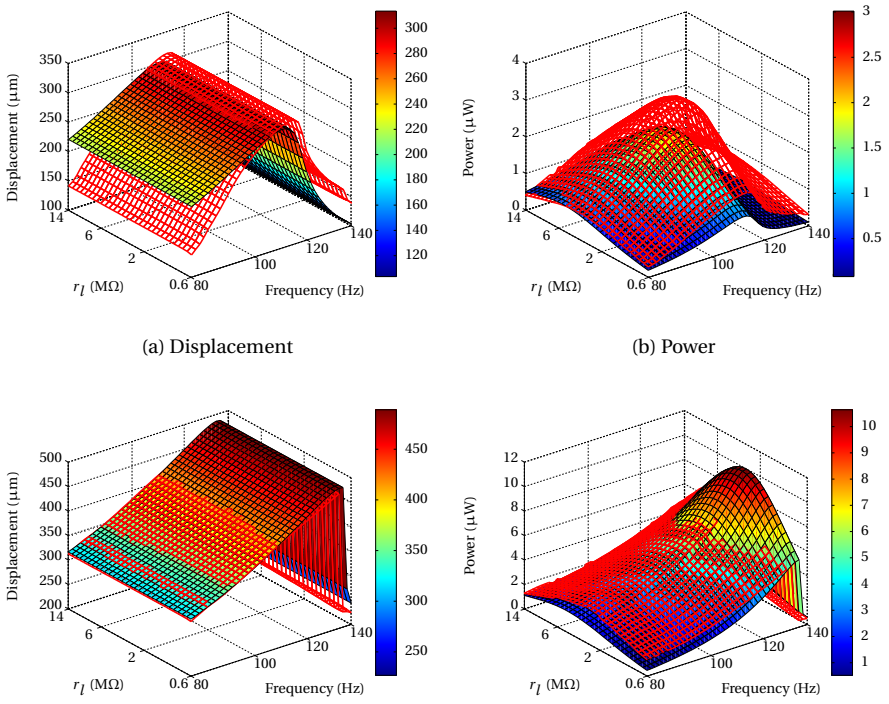

(a) Displacement

(b) Power

(c) Displacement

(d) Power

Figure 12: Comparison between experimental (red mesh) and optimized simulation (color scale) (a-b) at 30 m/s^2 and (c-d) at 60 m/s^2

5. Conclusion

An original membrane generator matching low frequency vibration energy harvesting applications is proposed. A complete theoretical model has been developed.

A prototype was realized and is investigated aiming at the validation of the theoretical model. In this first prototype, single layered P(VDF-TrFE) film is used. The mechanical tension effect induced by large deformation has been obtained using 4 g excitation amplitude. The experimental results prove that this expected hardening effect and its ensuing electrical power generation is captured by the model. The realized generator exhibits low resonant frequency (119.56 Hz), large bandwidth (40.28 Hz) and power density (158.33 $\mu W/cm^3$). However, unexpected additional voltage induced by the linear flexural mechanical response of the membrane is noted. An identified linear piezoelectric electromechanical coefficient is then added to complete the model. In the targeted acceleration scope of the generator (4 g and more), the model gives rather good predictive results with an error lower than 15 % for the chosen comparison criteria (peak power amplitude, frequency and load at the optimal point). At lower acceleration or away from the resonance frequency, the deviations between analytical modeling and experimental results increase. In these cases, the influence of the linear electromechanical coefficient β, which is thought to be due to geometrical defects, on the membranes responses is indeed higher. However, the origin of the linear coupling coefficient is not completely identified, but it explains the difference between the models and experiments at 3 g and 6 g acceleration levels. The electric generation for linear (low amplitude) responses calls for further investigations. The geometry of the membrane may present some flaws and has to be verified. The material constitutive relations were considered as linear. Though, initial prestress associated to the assembly procedure and the large deformation dynamic solicitations could lead to additional material nonlinear effect.

Based on the obtained proof of concept, dedicated studies are envisioned. A better repeatability of the assembly will have to be reached. Plastic material was used for the frame realization to ease the prototyping. More rigid and nonconductive material may be used. It would also improve the prestress control of the membrane. The damping will have to be lowered to increase the performance. To the authors' knowledge, most of the damping can be associated to the polymer membrane. However, different fluid will have to be tested to assess its contribution.

Furthermore, another architecture of electroactive membrane will be investigated to increase the power density. For instance, the diaphragms bending could be fully utilized using multi-layered piezoelectric film (bimorph structure) and two

dissociated electrode rings on the external faces of membrane stack. By doing this, the bending deformation can be exploited and lower acceleration magnitude could be focused on. Though, the expected increased stiffness may lead to higher column of fluid to keep the low frequency response advantage of the proposed architecture. A global optimization will then be necessary to aim at enhanced power density depending on the targeted application.

Acknowledgements

This work was supported by the Centre Technique des Industries Mécaniques (CETIM) and the Assemblée des Pays de Savoie (APS).

6. Bibliography

[1] J.A. Paradiso, Energy scavenging for mobile and wireless electronics, IEEE Pervasive Comput 4 (1) (2005) 18–27. doi:10.1109/MPRV.2005.9.

[2] S.P. Beeby, M.J. Tudor, N.M. White, Energy harvesting vibration sources for microsystems applications, Meas. Sci. Technol. 17 (12) (2006) R175–R195. doi:10.1088/0957-0233/17/12/R01.

[3] P.D. Mitcheson, E.M. Yeatman, G.K. Rao, A.S. Holmes, T.C. Green, Human and Machine Motion for Wireless Electronic Devices, Proc. IEEE 96 (9) (2008) 1457–1486. doi:10.1109/JPROC.2008.927494.

[4] S. Roundy, P.K. Wright, J. Rabaey, A study of low level vibrations as a power source for wireless sensor nodes, Comput. Commun., 26 (11) (2003) 1131–1144. doi:10.1016/S0140-3664(02)00248-7.

[5] I. Kuehne, D. Marinkovic, G. Eckstein, H. Seidel, A new approach for MEMS power generation based on a piezoelectric diaphragm, Sensors Actuators, A Phys. 142 (2008) 292–297. doi:10.1016/j.sna.2007.04.031.

[6] E. Minazara, D. Vasic, F. Costa, G. Poulin, Piezoelectric diaphragm for vibration energy harvesting., Ultrasonics 44 Suppl 1 (2006) e699–703. doi:10.1016/j.ultras.2006.05.141.

[7] X.-r. Chen, T.-q. Yang, W. Wang, X. Yao, Vibration energy harvesting with a clamped piezoelectric circular diaphragm, Ceram. Int. 38 (2012) S271–S274. doi:10.1016/j.ceramint.2011.04.099.

[8] S. Kim, Piezoelectric Energy Harvesting with a Clamped Circular Plate: Experimental Study, J. Intell. Mater. Syst. Struct. 16 (10) (2005) 855–863. doi:10.1177/1045389X05054043.

[9] S. Kim, Piezoelectric Energy Harvesting with a Clamped Circular Plate: Analysis, J. Intell. Mater. Syst. Struct. 16 (10) (2005) 847–854. doi:10.1177/1045389X05054044.

[10] C. Mo, L.J. Radziemski, W.W. Clark, Experimental validation of energy harvesting performance for pressure-loaded piezoelectric circular diaphragms, Smart Mater. Struct. 19 (7) (2010) 075010. doi:10.1088/0964-1726/19/7/075010.

[11] C. Mo, J. Davidson, W.W. Clark, Energy harvesting with piezoelectric circular membrane under pressure loading, Smart Mater. Struct. 23 (2014) 045005. doi:10.1088/0964-1726/23/4/045005.

[12] S. Rammohan, C. Ramya, S. Jayanth Kumar, Low frequency vibration energy harvesting using arrays of PVDF piezoelectric bimorphs, J. Inst. smart Struct. ans Syst. 3 (1) (2014) 18–27.

[13] M. Kato, K.-i. Kakimoto, Processing and energy-harvesting ability of (Na, K) NbO3 particle-dispersed fi brous polyvinylidene fl uoride multilayer composite, Mater. Lett. 156 (2015) 183–186. doi:10.1016/j.matlet.2015.05.019.

[14] Y. Jiang, S. Shiono, H. Hamada, Low-frequency energy harvesting using a laminated PVDF cantilever with a magnetic mass, Proc. PowerMEMS 2010 (2010) 375.

[15] R. Lockhart, R. Dauksevicius, A.V. Quintero, P. Janphuang, D. Briand, N.F. de Rooij, Flexible and Robust Multilayer Micro-Vibrational Harvesters for High Acceleration Environments, J. Phys. Conf. Ser. 476 (2013) 012113. doi:10.1088/1742-6596/476/1/012113.

[16] F. Formosa, A. Badel, H. Favrelière, Development of low frequency, insulating thick diaphragms for power MEMS applications, Sensors Actuators A Phys. 189 (2013) 370–379. doi:10.1016/j.sna.2012.09.018.

[17] Y.W. Kim, Y.S. Lee, S.H. Ko, Coupled vibration of partially fluid-filled cylindrical shells with ring stiffeners, J. Sound Vib. 276 (2004) 869–897. doi:10.1016/j.jsv.2003.08.008.

[18] S. Timoshenko, S. Woinowsky-Krieger, Theory of plates and shells, New York, 1959.

[19] M. Haterbouch, R. Benamar, Geometrically nonlinear free vibrations of simply supported isotropic thin circular plates, J. Sound Vib. 280 (3-5) (2005) 903–924. doi:10.1016/j.jsv.2003.12.051.

[20] K.S. Ramadan, D. Sameoto, S. Evoy, A review of piezoelectric polymers as functional materials for electromechanical transducers, Smart Mater. Struct. 23 (3) (2014) 033001. doi:10.1088/0964-1726/23/3/033001.